PHYSICAL REVIEW A **105**, 022622 (2022)

Optimization of a quantum control sequence for initializing a nitrogen-vacancy spin register

T. Chakraborty,[1,*] J. Zhang,[1] and D. Suter[1,2]
[1]*Fakultät Physik, Technische Universität Dortmund, D-44221 Dortmund, Germany*
[2]*Department of Physics and NMR Research Center, Indian Institute of Science Education and Research, Pune 411008, India*

(Received 5 July 2021; revised 20 December 2021; accepted 8 February 2022; published 24 February 2022)

Implementation of many quantum information protocols requires an efficient initialization of the quantum register. In the present paper, we optimize a population trapping protocol for initializing a hybrid spin register associated with a single nitrogen-vacancy (NV) center in diamond. We initialize the quantum register by polarizing the electronic and nuclear spins of the NV with a sequence of microwave, radio-frequency, and optical pulses. We use a rate equation model to explain the distribution of population under the effect of the optical pulses. The model is compared to the experimental data obtained by performing partial quantum state tomography. To further increase the spin polarization, we propose a recursive protocol with optimized optical pulses. We also discuss the role of the relative values of the nuclear- and electronic-spin pumping rate in achieving the maximum degree of spin polarization.

DOI: 10.1103/PhysRevA.105.022622

I. INTRODUCTION

A nitrogen atom replacing one carbon atom of a diamond lattice and an adjacent carbon vacancy site form a nitrogen-vacancy (NV) center in diamond, which is an optically active atomic defect center [1,2]. The NV center, having excellent quantum properties like long spin coherence time [3], offers a stable spin-photon interface [4,5], coherent optical transitions, and so on, which have been successfully applied in a number of aspects of the emerging field of quantum technology [6–8]. For instance, NV centers were used to demonstrate spin-photon entanglement with scalability [9], quantum teleportation [10], efficient implementation of quantum algorithms [11], entanglement distribution over a multinode quantum network [12], photonic quantum repeaters [13], quantum sensing platforms with remarkable sensitivity [14,15], and so on.

Having a large band gap (5.4 eV), diamond has an unoccupied conduction band which does not allow interaction of free electrons with the NV centers [16]. NV spins are not considerably sensitive to the lattice vibrations in diamond as the ground states of the NV centers do not possess an orbital degree of freedom. In addition, naturally abundant diamond crystals contain magnetic impurities of very low concentration (1.1% ^{13}C), and ultrapure single-crystal diamonds contain NVs with slowly dephasing spins [17]. Thus diamond, as a host, ensures that NV centers can be considered as isolated quantum systems, where the long-lived electronic and nuclear spins associated with NVs can act as quantum registers [18]. Several experiments demonstrated local control of the NV spins with high fidelity through initialization, coherent manipulation, and readout using optical, microwave (MW), and radio-frequency (RF) pulses [18–21].

Often for quantum operations, hybrid spin registers associated with NVs are exploited [18,21–24]. Commonly, these registers include vacancy electronic spins being coupled to the nuclear spins from ^{14}N or neighboring ^{13}C atoms [2]. For efficient implementation of several NV-based quantum information protocols, it is necessary that the initial state of the spin register has high purity. Hence, one needs to optimize methods which simultaneously polarize the electronic and nuclear spins of the NV center. Although it is straightforward to polarize the electronic spin by a significant amount through optical pumping [25], it does not allow polarization of the nuclear spins. Due to having an ultralong spin coherence time, nuclear spins are important candidates for storing and processing quantum information. Hence, to use nuclear spin as a resource in quantum protocols, it is necessary to perform the nuclear polarization strategically. In this context a number of techniques are reported. Polarization of ^{15}N nuclear spin is performed by accessing the excited-state level anticrossing for a single NV at room temperature [26]. By means of transferring polarization from electronic spins, hyperpolarization of ^{13}C nuclear-spin ensembles is achieved using a sequence of laser and microwave pulses, and by exploiting the fact that the nuclear-spin eigenstates do not have the same quantization axes in different electron-spin manifolds, which occurs because NV electron spin $S = 1$ [27]. Recently it was observed that the nuclear spin is depolarized on a slower timescale under 594-nm illumination compared to 532- or 520-nm light [24]. Moreover, bulk nuclear polarization around NV centers is achieved by applying laser induced dynamic nuclear polarization schemes [28–34].

In the present case, we initialize the spin register through polarizing the electronic and nuclear spins by applying a sequence of laser, MW, and RF pulses. We consider a hybrid two qutrit system where the vacancy electron is coupled to the ^{14}N nuclear spin, and perform the spin manipulation in a subspace of the spins, similar to an earlier protocol [23]. A good understanding of the laser induced population dynamics

---

[*] Present address: QuTech and Kavli Institute of Nanoscience, Delft University of Technology, 2600 GA Delft, The Netherlands.

among the relevant spin states is necessary for optimizing the polarization sequence. Hence, the present paper focuses on gaining insights into the effect of laser pumping on the NV electronic and nuclear spins. A detailed optimization of the spin control sequence is performed by formulating a rate equation model and the population dynamics of the relevant quantum states are investigated. Employing optically detected magnetic resonance spectroscopy techniques we perform partial state tomography and determine the occupation probabilities of all three nuclear-spin states in electronic-spin subspace $m_S = 0$. We have also performed simulations to test the efficiency of our sequence when it is implemented in an iterative way. Guided by numerical simulations, we optimize the duration of each laser pulse in the sequence.

The paper is organized as follows. First, we describe the system and the initialization sequence. Then we present the experimental results and compare them with the solution of the rate equation model. Finally, we present the results of the multicycle simulation.

II. SYSTEM AND POLARIZATION PROCEDURE

The experiments were performed in a home-built confocal microscope setup integrated with an electronic circuit which generates the necessary MW and RF signals for controlling the electronic and nuclear spins, as described in Ref. [21]. We chose the vacancy electronic spin $S = 1$ coupled with the ^{14}N nuclear spin $I = 1$ of an isolated NV center embedded in a 99.998% ^{12}C enriched diamond as the quantum register for our experiments. The system Hamiltonian, when the field is aligned along the NV axis, is

$$H = DS_z^2 - \gamma_e BS_z + PI_z^2 - \gamma_n BI_z + AS_zI_z. \tag{1}$$

S_z and I_z are the z components of the electronic and nuclear spins; the zero-field splitting is $D = 2.87$ GHz; electronic and nuclear gyromagnetic ratios are $\gamma_e = -28$ GHz T^{-1} and $\gamma_n = 3.1$ MHz T^{-1}, respectively; the nuclear quadrupole coupling $P = -4.95$ MHz; and the hyperfine coupling $A = -2.16$ MHz [21]. We performed the experiments in a magnetic field $B = 6.1$ mT along the symmetry axis of the NV.

Our initialization procedure relies on a population trapping (PT) protocol where by applying a number of π pulses we sequentially accumulate the population into the $m_I = 0$ state. For this purpose, we perform the spin manipulation in a subspace spanned by $m_s = 0, -1$ and $m_I = 0, \pm 1$. We write the states in the notation $|m_s, m_I\rangle$ in this paper. A coherent population trapping protocol couples an initial and a target state to an intermediate excited state by applying coherent electromagnetic fields, which trap the population in the superposition of the initial and the target states [35,36]. However, in our case, instead of applying coherent driving fields simultaneously, we sequentially apply MW, RF, and optical pulses to drive the population between the initial state $|0, \pm 1\rangle$ and the target state $|0, 0\rangle$ through certain intermediate states. Therefore, we term this method a "population trapping" protocol. Figure 1 schematically represents the PT pulse sequence. We illustrate the PT protocol later in this section. The relevant energy eigenstates of the six level system are shown in Fig. 1. The present sequence manipulates the spins associated with the NV$^-$ charge state. The transition frequencies and Rabi frequencies for the electronic and nuclear transitions, which we address in the sequence, are shown in Table I. In the beginning, a 5-μs-long laser pulse initializes the system into the bright ($m_s = 0$) state of the electron spin while the nuclear spin is fully depolarized. Now we aim to optimally polarize both the electron and nuclear spins by applying a combination of MW, RF, and laser pulses. We perform this task in two segments: through segment(seg)1 and seg2, we address the population associated with the $m_I = -1$ and $+1$ states in turn. Seg3 contains the pulses which we use for analyzing the resulting state. Seg1 includes a MW and an RF π pulse which drive the transitions $|0, -1\rangle \leftrightarrow |-1, -1\rangle$ and $|-1, -1\rangle \leftrightarrow |-1, 0\rangle$ polarizing the nuclear spin. These pulses generate electronic-spin–nuclear-spin entanglement and leave the electronic spin depolarized at the end of the sequence. To repolarize the electronic spin, we apply a second laser pulse. The effect of this laser pulse is primarily a polarization of the electron spin, but it also partly depolarizes the ^{14}N nuclear spin [21]. We therefore adjust the duration of the laser pulse to maximize the electronic- and nuclear-spin polarization. This task is performed by measuring the influence of the laser pulse duration on the population transfer dynamics and by interpreting the results using a rate equation model, which is discussed in the subsequent section.

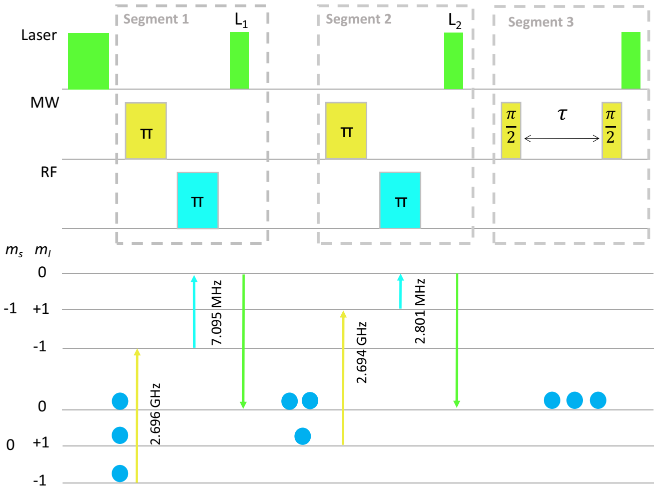

FIG. 1. Sequence of microwave (MW), radio frequency (RF), and 532-nm laser pulses used for initialization. The sequence contains three parts: segments 1 and 2 for addressing the nuclear spins $m_I = -1$ and $+1$, and segment 3 for measuring free-induction decay of the electronic spin. The energy levels with the relevant transitions are shown where the populations of the states are represented by filled circles.

TABLE I. Relevant transition frequencies and Rabi frequencies, that we use in our initialization sequence.

Transitions	Transition frequency	Rabi frequency
$\|0, -1\rangle \leftrightarrow \|-1, -1\rangle$	2.696 GHz	8.3 MHz
$\|0, +1\rangle \leftrightarrow \|-1, +1\rangle$	2.694 GHz	8.3 MHz
$\|-1, -1\rangle \leftrightarrow \|-1, 0\rangle$	2.801 MHz	3.87 kHz
$\|-1, +1\rangle \leftrightarrow \|-1, 0\rangle$	7.095 MHz	3.55 kHz

Seg2 transfers the population from $|0,+1\rangle$ to $|-1,0\rangle$ using a MW and an RF π pulse which act selectively on the transitions $|0,+1\rangle \leftrightarrow |-1,+1\rangle$ and $|-1,+1\rangle \leftrightarrow |-1,0\rangle$, and swap the populations between them. Next, in close analogy to seg1, we repolarize the electronic spin with a laser pulse and optimize its duration. A proper optimization of the control pulses maximizes the population of the $|00\rangle$ state. The optimization of the laser pulses and the experimental analysis of the final populations of the relevant states are described in the next section.

III. EXPERIMENTAL RESULTS AND COMPARISON WITH THE RATE EQUATION MODEL

We implement the proposed initialization protocol and perform the optimization of the L_1 and L_2 laser pulses in two steps. After polarizing the electronic spin using the 5-μs laser pulse, we test and optimize seg1, and analyze the resulting populations of the states through the measurement protocol of seg3. During this process, we do not implement seg2. To investigate the redistribution of population under the influence of the laser pulse L_1, we run seg1 for different values of the laser pulse duration, and perform partial state tomography. This is done by capturing Ramsey-type free-induction decays (FIDs) of the electronic spin using the control sequence in seg3. In seg3, the FID sequence contains two $\pi/2$ MW pulses which are separated by a free evolution time τ and are resonant between the $m_s = 0$ and -1 levels. The first $\pi/2$ pulse creates a coherent superposition of the $|m_s = 0\rangle$ and $|m_s = -1\rangle$ states, which evolves for a time τ. The coherence is then converted into population difference by the second $\pi/2$ pulse and read out using a laser pulse of 300-ns duration. We apply hard (high power) $\pi/2$ pulses such that all three nuclear-spin-conserving transitions between $m_s = 0$ and -1 are excited. A Fourier transform of the time domain FID data allows us to capture spectral amplitudes associated with the $|m_I = 0, \pm 1\rangle$ states in the frequency domain. Thus the spectra contain three lines the amplitudes A_{m_I} of which are proportional to the difference of populations between the $m_S = 0$ and -1 states:

$$A_{m_I} = P_{|0,m_I\rangle} - P_{|-1,m_I\rangle}. \tag{2}$$

To explain the laser induced population transfer dynamics among the six energy levels of the spin register, we formulate a rate equation model. We define a column matrix representing the populations of the six states and call it the population vector $\vec{P}$. We express the rate equation in the following form:

$$\frac{d\vec{P}}{dt} = M(k_s, k_I)\vec{P}. \tag{3}$$

Since the spin manipulation is performed in the subspace spanned by the $|m_S = 0, -1\rangle \otimes |m_I = 0, \pm 1\rangle$ states, the $m_S = +1$ state remains unoccupied throughout the spin control sequence. The populations of the states in $\vec{P}$ follow the order $(m_s, m_I) = (0, -1; 0, +1; 0, 0; -1, -1; -1, +1; -1, 0)$, which is the same order for the energy levels shown in Fig. 1. The rate matrix M describes the transfer of population between the states due to the effect of the laser pulse and is given in the Appendix. We assume that the electronic spin changes from $m_S = -1$ to 0 with a rate of k_s and the nuclear spin changes between any of the states $|m_I = 0, \pm 1\rangle$ at a rate k_I. Assuming that the sum of the populations is unity, the spectral amplitudes for the ^{14}N nuclear spins $m_I = 0$ and ± 1 are normalized with reference to the initial-state amplitudes experimentally measured after applying the 5-μs-long laser pulse, which equally populates all nuclear-spin sublevels. Thus, the normalized population vector for this state is $\vec{P} = \frac{1}{3}(1, 1, 1, 0, 0, 0)$. The MW and RF pulses of seg1 ideally convert this into $\vec{P} = \frac{1}{3}(0, 1, 1, 0, 0, 1)$, which is the initial condition for the dynamics during the laser pulse. The solution of Eq. (3) for this initial condition is given in Eq. (A1) in the Appendix.

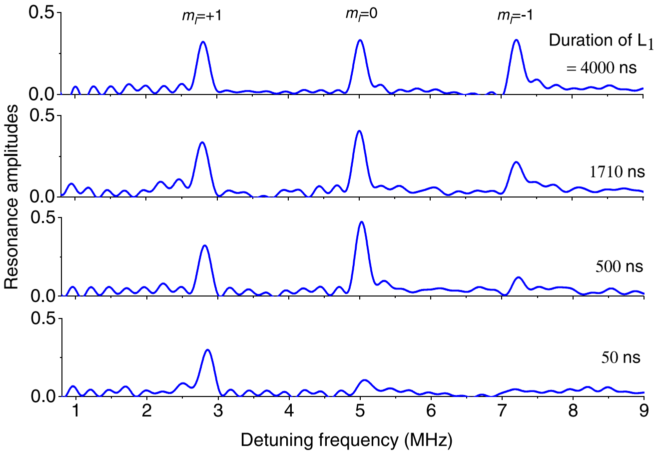

FIG. 2. Electron-spin-resonance spectra obtained by Fourier transforming the free-induction-decay data for the electronic spin. The four spectra correspond to four different durations of the laser pulse L_1 in seg1. The amplitudes of the three lines in the spectra are proportional to the populations of the three nuclear-spin states as marked in the figure.

Figure 2 exhibits four experimental spectra measured after the implementation of seg1 with durations of 50, 500, 1700, and 4000 ns of the laser pulse L_1. The spectra consist of three lines associated with the nuclear-spin states $m_I = 0$ and ± 1, which are separated by the NV hyperfine interaction. The MW and RF pulses in seg1 do not control the population of the $|0,+1\rangle$ state. Thus it maintains its initial population of 1/3 after seg1. For the shortest duration of the L_1 pulse (50 ns), the electron spin does not repolarize significantly. Accordingly, the $m_I = 0$ states in the $m_s = 0$ and -1 subspaces have almost equal population, resulting in a very small amplitude A_0 of the $m_I = 0$ line in the spectrum. However, with increasing the duration of the L_1 pulse, the population of the $|m_I = 0, m_s = 0\rangle$ state increases, as the nuclear spin is mostly unaffected while the electronic spin is transferred from $m_S = -1$ to 0. If the laser-pulse duration is increased further, the nuclear spin becomes depolarized. Figure 2 shows that the three lines have equal amplitudes when the duration of L_1 is 4 μs.

The evolution of the amplitudes A_0 and $A_{\pm 1}$ of the three spectral lines, which are proportional to the population of the three nuclear-spin states $m_I = 0$ and ± 1, respectively, as shown in Eq. (2), and the total population of the three nuclear-spin states in the $m_S = 0$ subspace are shown in Fig. 3. The amplitudes increase with increasing pulse duration. A_0 reaches a maximum when the duration of the L_1 pulse is 500 ns. The

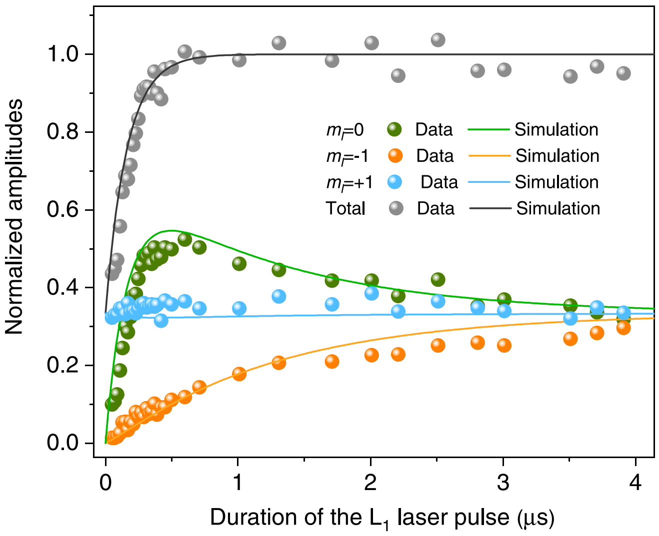

FIG. 3. The variation of spectral amplitudes that correspond to the populations of the nuclear-spin states $m_I = 0, \pm 1$ and their sum as a function of the duration of the laser pulse L_1 in seg1. The solid lines represent the simulation using the rate equation model. We used $1/k_S = 0.27$ μs and $1/k_I = 4.76$ μs [21].

population of all six states after seg1 can be obtained by substituting $t = 500$ ns in Eq. (A1). The population of the $|0, 0\rangle$ state is 0.55 ± 0.02, taking into account the uncertainties in k_s and k_I. The experimental value of A_0 for $t = 500$ ns is 0.5. This optimized pulse allows us to obtain the maximum polarization of the electron spin with the minimum loss of nuclear-spin polarization. When the duration of the L_1 pulse reaches 4 μs, the total population of the $m_S = 0$ state reaches unity which signifies complete electronic polarization. A_0 and A_{-1} converge to 1/3 which indicates complete nuclear-spin depolarization. A_{+1} maintains a constant value of 1/3 for all durations of the laser pulse. The amplitudes simulated using our rate equation model are in excellent agreement with the experimental data. Under our experimental conditions, k_s and k_I are similar to the values reported in Ref. [21].

Next, we set the duration of the L_1 pulse to 500 ns and proceed with the experiments using the sequence of pulses contained in seg2. At the start of seg2, the populations are $\vec{P} = (0.07, 0.33, 0.55, 0, 0, 0.05)$, as obtained by substituting 500 ns in Eq. (A1). In this stage, the MW and RF pulses drive the transitions $|0, +1\rangle \leftrightarrow |-1, +1\rangle$ and $|-1, +1\rangle \leftrightarrow |-1, 0\rangle$, respectively, and the resulting population vector is $\vec{P} = (0.07, 0, 0.55, 0, 0.05, 0.33)$. Using this as the initial condition, we again solve the rate equation model for the second laser pulse L_2. The analytical expression for the solution is shown in Eq. (A2) in the Appendix.

Four spectra measured for 60-, 460-, 1410-, and 4000-ns duration of the laser pulse L_2 are shown in Fig. 4. Similar to the earlier case, due to electron-spin polarization, an increase in pulse duration increases the population difference between the states $|0, 0\rangle$ and $|-1, 0\rangle$. The amplitude A_0 reaches its maximum for a pulse duration of 460 ns. The maximum population of the $|0, 0\rangle$ state after seg2 is 0.71 ± 0.02 obtained using Eq. (A2) for a duration of L_2 of 460 ns. We obtain $A_0 = 0.72$ for $t = 460$ ns from the experimental data. The evolution of the amplitudes with the laser pulse duration can better be observed in Fig. 5. The nuclear spin starts to depolarize, populating the $m_I = \pm 1$ states as the laser pulse duration becomes longer, and eventually the nuclear spin depolarizes completely. The rate equation model is well consistent with experimental data as shown in Fig. 5.

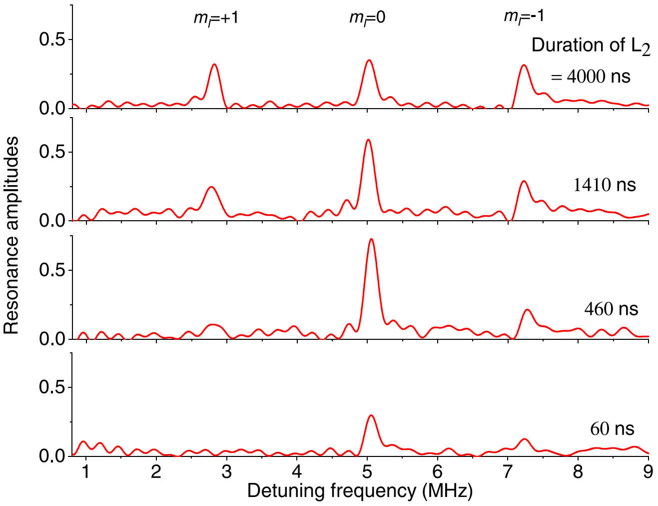

FIG. 4. Fourier transforms of free-induction decays of the electronic spin for four different durations of L_2. The spectra show three peaks for the three nuclear-spin states $m_I = 0, \pm 1$ of ^{14}N.

IV. ITERATION TO ENHANCE PURITY

Earlier experimental studies of population transfer dynamics have shown that laser induced depolarization of the nuclear spin limits the overall purity [21,24]. In this section we show that it is possible to enhance the polarization of the hybrid spin register beyond the values obtained for a single cycle in

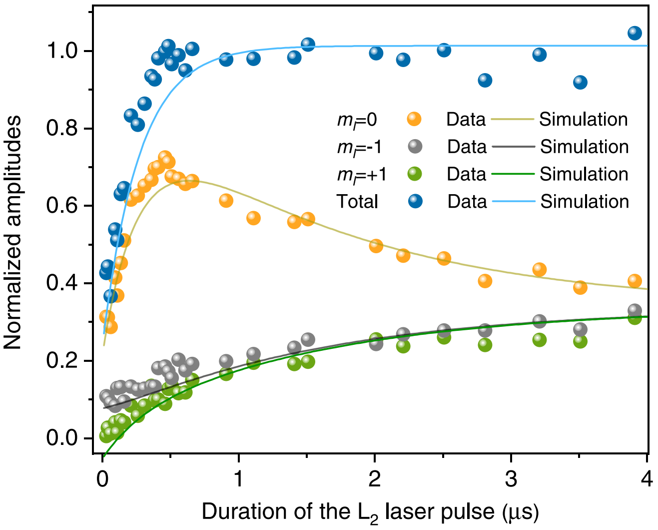

FIG. 5. Amplitudes of the three resonance lines corresponding to the populations of $m_I = 0, \pm 1$, together with their sum, as a function of the laser-pulse (L_2) duration. The simulations performed using the rate equation model (with $1/k_S = 0.27$ μs and $1/k_I = 4.76$ μs [21]) are shown by the solid curves.

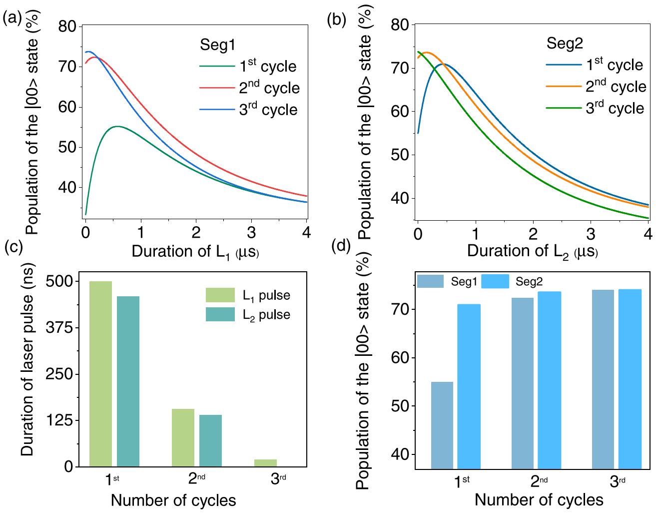

FIG. 6. Resulting population of the $|0, 0\rangle$ state after each cycle for (a) seg1 and (b) seg2. (c) Optimized duration of the laser pulses for three cycles for seg1 and seg2. (d) Purity after each cycle for seg1 and seg2.

TABLE II. Simulated values of the laser pulse duration and population of the $|0, 0\rangle$ state after each of the three cycles for seg1 and seg2.

Number of cycles	Duration of L_1(ns)	$P_{\|0,0\rangle}$ after seg1 (%)	Duration of L_2(ns)	$P_{\|0,0\rangle}$ after seg2 (%)
1	500	55	460	70.9
2	156	72.3	140	73.5
3	20	74	0	74

Sec. III, when MW, RF, and properly optimized 532-nm laser pulses are applied in an iterative way. We rely on the idea that when we apply the initialization sequence [seg1 + seg2] as shown in Fig. 1 for multiple cycles, each subsequent cycle uses the final populations of a given cycle as the initial state. Thus, when a cycle starts with an improved purity of the target $|0, 0\rangle$ state, the purity of the state is enhanced further at the end of the cycle. We experimentally have implemented the sequence [seg1 + seg2] $\times N$ for $N = 1$ to 5 and have analyzed the resulting state using seg3. However, in this way the resulting gain in the purity of the $|0, 0\rangle$ state is very small ($\approx$1%). An additional improvement can be obtained by adjusting the durations of the laser pulses independently, using the rate equation discussed in Sec. III for each pulse depending on the relevant initial states. Below we explain a protocol and demonstrate the results of the simulation we have performed.

We simulate the implementation of seg1 and seg2 in an iterative way: we simulate the population redistribution for a sequence [seg1 + seg2] $\times N$ where the durations of the pulses L_1 and L_2 are optimized for each cycle. For the first cycle we choose the duration of the L_1 and L_2 pulses as 500 and 460 ns as the resonance amplitudes for the nuclear spin $m_I = 0$ are maximum for these values (Figs. 3 and 5, respectively). For the second cycle, we consider the experimentally obtained final population after the first cycle as the initial state and solve the rate equation model for $L_1$and L_2 pulses. In this cycle, we observe that maximum transfer of population to the $|0, 0\rangle$ state occurs when the durations of the $L_1$and L_2 pulses are 156 and 140 ns. In this similar way, we solve the rate equation for the third cycle. The variations of the population of the $|0, 0\rangle$ state as a function of the duration of L_1 and L_2 for three cycles are shown in Figs. 6(a) and 6(b). The optimized duration of the laser pulses and the obtained purity $P_{|0,0\rangle}$ for three cycles are shown in Figs. 6(c) and 6(d). Table II summarizes these values for both segments. Moreover, we also have simulated the population redistribution for a sequence [(seg1)$\times N$ + (seg2)$\times N$] where we first optimize the duration of the laser pulses for three consecutive cycles of seg1 and then we do a similar task for seg2. However, this method could enhance the purity only by 0.9% compared to the pulse sequence shown in Fig. 1.

The experimental results obtained by applying the full initialization scheme depicted in Fig. 1 and the above results of multicycle simulations indicate that the relative values of the spin pumping rates limit the achievable purity of the target $|0, 0\rangle$ state. To investigate the influence of the relative values of k_I and k_S on the maximum achievable population of the $|0, 0\rangle$ state, we perform additional simulations. For this purpose, we denote the ratio of the nuclear- to electronic-spin pumping rate as $r = k_I/k_S$. r is varied from 0 to 0.5: $r = 0$, 0.056, and 0.5 signify the scenarios where the nuclear depolarization is zero, equal to and considerably stronger than the experimentally obtained value, respectively. We keep the value of $1/k_S$ fixed at 0.27 μs throughout this analysis. Assuming $\vec{P} = \frac{1}{3}(1, 1, 1, 0, 0, 0)$ as the initial condition, we implement seg1 and calculate $P_{|0,0\rangle}$. We show $P_{|0,0\rangle}$ as a function of the duration t_{L_1} of the L_1 pulse and r in Fig. 7. When the nuclear spin is not depolarized ($r = 0$), the L_1 pulse does not populate the $|0, \pm1\rangle$ states and $P_{|0,0\rangle}$ saturates at its maximum value of 2/3 with increasing laser-pulse duration t_{L_1}. $P_{|0,-\rangle}$ and $P_{|0,1\rangle}$ maintain their initial values of 0 and 1/3 as t_{L_1} changes, which can be see in Figs. 7(b) and 7(c). When $r = 0.056$, the variation of $P_{|0,0\rangle}$ and $P_{|0,\pm1\rangle}$ with t_{L_1} is similar to what we observe in Fig. 3. However, when $r > 0.056$, the maximum attainable polarization after seg1 decreases and $P_{|0,-1\rangle}$ increases. For instance, when $r = 0.5$, the maximum value of $P_{|0,0\rangle}$ is 0.497 when $t_{L_1} = 190$ ns. Now, similar to the experimental case, we assume the initial condition $\vec{P} = (0.07, 0.33, 0.55, 0, 0, 0.05)$ (for $r = 0.056$ and $t_{L_1} = 500$ ns in seg1) and simulate the population of the $P_{|0,0\rangle}$ and $P_{|0,\pm1\rangle}$ states after seg2 as a function of r and the duration of the L_2 pulse t_{L_2}. Figure 7(d) shows that when $r = 0$, the attainable population of the $|0, 0\rangle$ state is maximum (0.87) and it decreases as r increases: $P_{|0,0\rangle} = 0.55$ when $r = 0.5$. For higher values of r, the population of the states $|0, -1\rangle$ and $|0, 1\rangle$ increases, as shown in Figs. 7(e) and 7(f). For $r = 0$, as t_{L_2} increases, $P_{|0,1\rangle}$ saturates at 0.05 as the residual population in state $|-1, 1\rangle$ caused by the seg1 pulses is transferred to $|0, 1\rangle$ by the L_2 pulse. Furthermore, we estimate $P_{|0,0\rangle}$ after seg2 with r being 0 and 0.5 for seg1, as shown in Figs. 8(a) and 8(b) in the Appendix. Figures 8(a) and 8(b) show that when there is no nuclear depolarization during seg1 and seg2, the total population can be transferred to $|0, 0\rangle$. However if the nuclear depolarization rate is significantly higher ($r = 0.5$) in

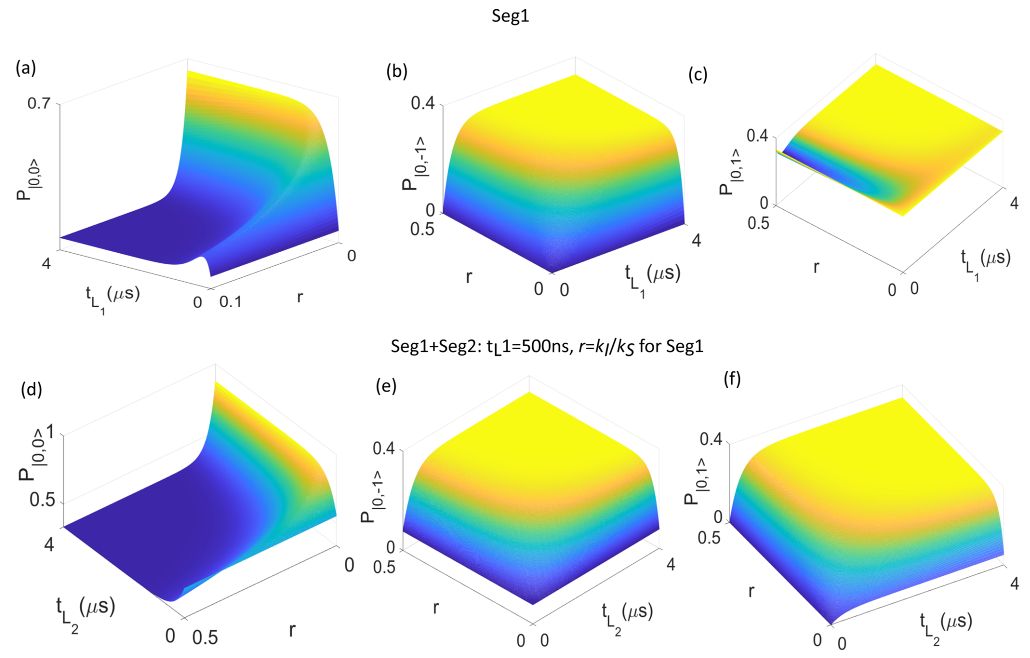

FIG. 7. Dependence of (a) $P_{|0,0\rangle}$, (b) $P_{|0,-1\rangle}$, and (c) $P_{|0,1\rangle}$ on the duration t_{L_1} of the laser pulse L_1 and $r(k_I/k_S)$ after the first segment. (d) $P_{|0,0\rangle}$, (e) $P_{|0,-1\rangle}$, and (f) $P_{|0,1\rangle}$ as a function of t_{L_2} and r after both segments, using $t_{L_1} = 500$ ns and $r = 0.056$ for seg1.

seg1 and seg2, the final purity of the $|0,0\rangle$ state is limited to $1/3$. Thus, the above simulations show that the optically induced nuclear depolarization is the key factor in limiting the final purity of the $|0,0\rangle$ state achievable using our population trapping protocol.

V. DISCUSSIONS AND CONCLUSION

The present paper demonstrates a detailed optimization procedure for initializing a hybrid quantum spin register associated with a single NV center by performing the spin manipulation in a reduced subspace of the spins. We apply a series of MW and RF pulses to swap the electronic- and nuclear-spin polarization and laser pulses for optically pumping the electronic spin. The durations of the laser pulses are optimized in such a way that we maximize the electronic- and nuclear-spin polarization: nonresonant optical pumping polarizes the electronic spin on fast timescales, which provides the mechanism for polarizing the electronic spin, but depolarizes the nuclear spin on longer timescales. We select the pulse duration between these two timescales that maximizes the per-cycle nuclear polarization. For this purpose, we formulate a rate equation model and investigate the polarization dynamics as a function of the duration of the laser pulse. By performing partial state tomography we experimentally determine the population of the relevant eigenstates.

We follow an approach developed in Ref. [21] to optimize the laser pulse duration. However, in this case we have applied a different polarization method which is based on a population trapping protocol. With this protocol, we access the subspace spanned by $|m_S = 0, -1\rangle \otimes |m_I = 0, \pm1\rangle$ states and sequentially populate the target state $|0,0\rangle$. For this purpose, a number of MW, RF, and optical pulses are employed to drive the population from the initial state $|0,\pm1\rangle$ to the target state through certain intermediate states in $m_S = -1$ subspace. We have optimized the optical pumping processes to maximize the spin polarization. To describe the present experimental results, we have used a rate equation model which explains laser induced redistribution of the population among the six spin levels. Furthermore, to reduce the nuclear depolarization, we have formulated a recursive method where in each cycle the laser pulses perform the optical pumping in an optimum way. Our simulation shows that when multiple cycles of the control sequence, with each cycle having an optimum laser pulse duration, are implemented, an enhancement of the polarization can be achieved.

A number of factors limit the maximum achievable spin polarization. By performing simulations we conclude that the relative values of the nuclear and electronic pumping rates limit the maximum degree of spin polarization that can be obtained using the present PT method. Another limiting factor is the maximum achievable polarization of the electronic spin through optical pumping, which is ≈80% [25]. An important contribution to losing nuclear-spin polarization is the charge state conversion dynamics of the NV center. The two charge states have different hyperfine interactions. Thus, switching from one charge state to another can result in nuclear depolarization [21]. Further studies are required for a better understanding of this mechanism.

Initializing a quantum register to an eigenstate is important for implementation of quantum information tasks. In these protocols, optical control of the spins plays a significant role. The present results of the optimization of the optical control pulses can help developing efficient spin manipulation protocols. One advantage of our method is that the spin control can be performed in an arbitrary magnetic field. We have presented the results of the initialization experiment and multicycle simulations for an NV spin register. However, this spin manipulation approach is general. Hence, for other atomic defect centers in diamond which has optically addressable spin transitions, a similar method can be formulated.

ACKNOWLEDGMENTS

This project has received funding from the European Union's Horizon 2020 research and innovation program under Grant No. 828946. The work was also supported by the MERCUR (Mercator Research Center Ruhr) foundation through Grant No. Pr-2013-0003.

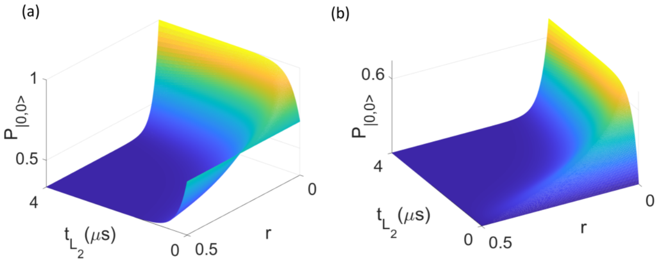

FIG. 8. Dependence of $P_{|0,0\rangle}$ on t_{L_2} and r after seg2 with (a) $r = 0$, $t_{L_1} = 4000$ ns and (b) $r = 0.5$, $t_{L_1} = 470$ ns in seg1.

APPENDIX

During the optical pulse, the redistribution of the populations $\vec{P}$ can be described as

$$\frac{d\vec{P}}{dt} = M(k_s, k_I)\vec{P},$$

where the matrix $M(k_S, k_I)$ of rate constants is

$$M(k_S, k_I) = \begin{bmatrix} -2k_I & k_I & k_I & k_S & 0 & 0 \\ k_I & -2k_I & k_I & 0 & k_S & 0 \\ k_I & k_I & -2k_I & 0 & 0 & k_S \\ 0 & 0 & 0 & -k_S & 0 & 0 \\ 0 & 0 & 0 & 0 & -k_S & 0 \\ 0 & 0 & 0 & 0 & 0 & -k_S \end{bmatrix}.$$

As discussed in the main text, the basis states are $(m_s, m_I) = (0, -1; 0, +1; 0, 0; -1, -1; -1, +1; -1, 0)$. The constants k_I and k_S describe the rates at which the electronic- and nuclear-spin polarizations are changed. Under our experimental conditions, $1/k_S = 0.27$ μs and $1/k_I = 4.76$ μs [21].

In seg1 the solution obtained for the initial condition $\vec{P}(0) = \frac{1}{3}(0, 1, 1, 0, 0, 1)$ is

$$\vec{P}_{\text{seg1}}(t) = \frac{1}{3}\left[1 - \frac{k_I(e^{-k_S t} - e^{-3k_I t})}{(3k_I - k_S)}, \quad 1 - \frac{(2k_I - k_S)e^{-3k_I t} + k_I e^{-k_S t}}{(3k_I - k_S)}, \right. \\ \left. 1 - \frac{(k_I - k_S)e^{-k_S t} + (k_s - k_I)e^{-3k_I t}}{(3k_I - k_S)}, \quad 0, 0, e^{-k_S t}\right]. \tag{A1}$$

For initial condition $\vec{P}(0) = (0.07, 0, 0.55, 0, 0.05, 0.33)$ in seg2, the solution is

$$\vec{P}_{\text{seg2}}(t) = \left[0.34 + \frac{e^{-3k_I t}(0.26k_S - 0.4k_I) - 0.38k_I e^{-k_S t}}{3k_I - k_S}, \right. \\ 0.34 - \frac{e^{-k_S t}(0.38k_I - 0.05k_S) + e^{-3k_I t}(0.63k_I - 0.29k_S)}{3k_I - k_S}, \\ \left. 0.34 + \frac{e^{-3k_I t}(1.03k_I - 0.55k_S) - e^{-k_S t}(0.38k_I - 0.33k_S)}{3k_I - k_S}, \quad 0, 0.05e^{-k_S t}, 0.33e^{-k_S t}\right]. \tag{A2}$$

The variation of $P_{|0,0\rangle}$ with r and t_{L_2} after both segments is shown in Fig. 8 for two different conditions of seg1: (a) $r = 0$, $t_{L_1} = 4000$ ns and (b) $r = 0.5$, $t_{L_1} = 470$ ns.

---

[1] F. Jelezko and J. Wrachtrup, Phys. Status Solidi A **13**, 3207 (2006).

[2] D. Suter and F. Jelezko, Prog. Nucl. Magn. Reson. Spectrosc. **98**, 50 (2017).

[3] G. Balasubramanian, P. Neumann, D. Twitchen, M. Markham, R. Kolesov, N. Mizuochi, J. Isoya, J. Achard, J. Beck, J. Tissler *et al.*, Nat. Mater. **8**, 383 (2009).

[4] A. Sipahigil, M. L. Goldman, E. Togan, Y. Chu, M. Markham, D. J. Twitchen, A. S. Zibrov, A. Kubanek, and M. D. Lukin, Phys. Rev. Lett. **108**, 143601 (2012).

[5] H. Bernien, L. Childress, L. Robledo, M. Markham, D. Twitchen, and R. Hanson, Phys. Rev. Lett. **108**, 043604 (2012).

[6] S. Pezzagna and J. Meijer, Appl. Phys. Rev. **8**, 011308 (2021).

[7] L. Childress and R. Hanson, MRS Bull. **38**, 134 (2013).

[8] N. Fabbri and S. Hernández-Gómez, Frontiers in Physics **8**, 652 (2021).

[9] R. Vasconcelos, S. Reisenbauer, C. Salter, G. Wachter, D. Wirtitsch, J. Schmiedmayer, P. Walther, and M. Trupke, npj Quantum Inf. **6**, 1 (2020).

[10] W. Pfaff, B. J. Hensen, H. Bernien, S. B. van Dam, M. S. Blok, T. H. Taminiau, M. J. Tiggelman, R. N. Schouten, M. Markham, D. J. Twitchen *et al.*, Science **345**, 532 (2014).

[11] J. Zhang, S. S. Hegde, and D. Suter, Phys. Rev. Lett. **125**, 030501 (2020).

[12] M. Pompili, S. L. Hermans, S. Baier, H. K. Beukers, P. C. Humphreys, R. N. Schouten, R. F. Vermeulen, M. J. Tiggelman, L. dos Santos Martins, B. Dirkse *et al.*, Science **372**, 259 (2021).

[13] K. Nemoto, M. Trupke, S. J. Devitt, B. Scharfenberger, K. Buczak, J. Schmiedmayer, and W. J. Munro, Sci. Rep. **6**, 1 (2016).

[14] C. L. Degen, F. Reinhard, and P. Cappellaro, Rev. Mod. Phys. **89**, 035002 (2017).

[15] R. Schirhagl, K. Chang, M. Loretz, and C. L. Degen, Annu. Rev. Phys. Chem. **65**, 83 (2014).

[16] J. A. Larsson and P. Delaney, Phys. Rev. B **77**, 165201 (2008).

[17] T. Chakraborty, F. Lehmann, J. Zhang, S. Borgsdorf, N. Wöhrl, R. Remfort, V. Buck, U. Köhler, and D. Suter, Phys. Rev. Materials **3**, 065205 (2019).

[18] M. G. Dutt, L. Childress, L. Jiang, E. Togan, J. Maze, F. Jelezko, A. Zibrov, P. Hemmer, and M. Lukin, Science **316**, 1312 (2007).

[19] L. Childress, M. G. Dutt, J. Taylor, A. Zibrov, F. Jelezko, J. Wrachtrup, P. Hemmer, and M. Lukin, Science **314**, 281 (2006).

[20] T. Gaebel, M. Domhan, I. Popa, C. Wittmann, P. Neumann, F. Jelezko, J. R. Rabeau, N. Stavrias, A. D. Greentree, S. Prawer *et al.*, Nat. Phys. **2**, 408 (2006).

[21] T. Chakraborty, J. Zhang, and D. Suter, New J. Phys. **19**, 073030 (2017).

[22] J. Wrachtrup and F. Jelezko, J. Phys.: Condens. Matter **18**, S807 (2006).

[23] D. Pagliero, A. Laraoui, J. D. Henshaw, and C. A. Meriles, Appl. Phys. Lett. **105**, 242402 (2014).

[24] K. Rama Koteswara Rao, Y. Wang, J. Zhang, and D. Suter, Phys. Rev. A **101**, 013835 (2020).

[25] L. Robledo, H. Bernien, T. Van Der Sar, and R. Hanson, New J. Phys. **13**, 025013 (2011).

[26] V. Jacques, P. Neumann, J. Beck, M. Markham, D. Twitchen, J. Meijer, F. Kaiser, G. Balasubramanian, F. Jelezko, and J. Wrachtrup, Phys. Rev. Lett. **102**, 057403 (2009).

[27] G. A. Álvarez, C. O. Bretschneider, R. Fischer, P. London, H. Kanda, S. Onoda, J. Isoya, D. Gershoni, and L. Frydman, Nat. Commun. **6**, 8456 (2015).

[28] J. Scheuer, I. Schwartz, Q. Chen, D. Schulze-Sünninghausen, P. Carl, P. Höfer, A. Retzker, H. Sumiya, J. Isoya, B. Luy *et al.*, New J. Phys. **18**, 013040 (2016).

[29] J. P. King, K. Jeong, C. C. Vassiliou, C. S. Shin, R. H. Page, C. E. Avalos, H.-J. Wang, and A. Pines, Nat. Commun. **6**, 1 (2015).

[30] A. Ajoy, R. Nazaryan, K. Liu, X. Lv, B. Safvati, G. Wang, E. Druga, J. Reimer, D. Suter, C. Ramanathan *et al.*, Proc. Natl. Acad. Sci. USA **115**, 10576 (2018).

[31] A. Ajoy, K. Liu, R. Nazaryan, X. Lv, P. R. Zangara, B. Safvati, G. Wang, D. Arnold, G. Li, A. Lin *et al.*, Sci. Adv. **4**, eaar5492 (2018).

[32] A. Ajoy, B. Safvati, R. Nazaryan, J. Oon, B. Han, P. Raghavan, R. Nirodi, A. Aguilar, K. Liu, X. Cai *et al.*, Nat. Commun. **10**, 1 (2019).

[33] P. R. Zangara, S. Dhomkar, A. Ajoy, K. Liu, R. Nazaryan, D. Pagliero, D. Suter, J. A. Reimer, A. Pines, and C. A. Meriles, Proc. Natl. Acad. Sci. USA **116**, 2512 (2019).

[34] A. Ajoy, R. Nazaryan, E. Druga, K. Liu, A. Aguilar, B. Han, M. Gierth, J. T. Oon, B. Safvati, R. Tsang *et al.*, Rev. Sci. Instrum. **91**, 023106 (2020).

[35] P. Jamonneau, G. Hétet, A. Dréau, J.-F. Roch, and V. Jacques, Phys. Rev. Lett. **116**, 043603 (2016).

[36] L. Nicolas, T. Delord, P. Jamonneau, R. Coto, J. Maze, V. Jacques, and G. Hétet, New J. Phys. **20**, 033007 (2018).